

Article

Enhancement of $Y_{5-x}Pr_xSb_{3-y}M_y$ ($M = Sn, Pb$) Electrodes for Lithium- and Sodium-Ion Batteries by Structure Disordering and CNTs Additives

Volodymyr Pavlyuk^{1,2,*} , Wojciech Ciesielski¹, Nazar Pavlyuk^{1,2}, Damian Kulawik¹, Agnieszka Balińska¹ and Karolina Kluziak¹

- ¹ Institute of Chemistry, Faculty of Science and Technology, Częstochowa Jan Długosz University, al. Armii Krajowej 13/15, 42200 Częstochowa, Poland; wc@ujd.edu.pl (W.C.); nazar.pavlyuk@gmail.com (N.P.); d.kulawik@ujd.edu.pl (D.K.); a.balinska@ujd.edu.pl (A.B.); karolina_kluziak@o2.pl (K.K.)
- ² Department of Inorganic Chemistry, Ivan Franko Lviv National University, Kyryla i Mefodia 6, 79005 Lviv, Ukraine
- * Correspondence: v.pavlyuk@ujd.edu.pl

Abstract: The maximally disordered (MD) phases with the general formula $Y_{5-x}Pr_xSb_{3-y}M_y$ ($M = Sn, Pb$) are formed with partial substitution of Y by Pr and Sb by Sn or Pb in the binary Y_5Sb_3 compound. During the electrochemical lithiation and sodiation, the formation of $Y_{5-x}Pr_xSb_{3-y}M_yLi_z$ and $Y_{5-x}Pr_xSb_{3-y}M_yNa_z$ maximally disordered–high entropy intermetallic phases (MD-HEIP), as the result of insertion of Li/Na into octahedral voids, were observed. Carbon nanotubes (CNT) are an effective additive to improve the cycle stability of the $Y_{5-x}Pr_xSb_{3-y}M_y$ ($M = Sn, Pb$) anodes for lithium-ion (LIBs) and sodium-ion batteries (SIBs). Modification of $Y_{5-x}Pr_xSb_{3-y}M_y$ alloys by carbon nanotubes allowed us to significantly increase the discharge capacity of both types of batteries, which reaches $280 \text{ mAh} \cdot \text{g}^{-1}$ (for LIBs) and $160 \text{ mAh} \cdot \text{g}^{-1}$ (for SIBs), respectively. For $Y_{5-x}Pr_xSb_{3-y}Pb_y$ alloys in which antimony is replaced by lead, these capacities are slightly smaller and are $270 \text{ mAh} \cdot \text{g}^{-1}$ (for LIBs) and $155 \text{ mAh} \cdot \text{g}^{-1}$ (for SIBs), respectively. Results show that structure disordering and CNT additives could increase the electrode capacities up to 30% for LIBs and up to 25% for SIBs.

Keywords: alloys; batteries; electrochemistry of materials; solid state electrochemistry



Citation: Pavlyuk, V.; Ciesielski, W.; Pavlyuk, N.; Kulawik, D.; Balińska, A.; Kluziak, K. Enhancement of $Y_{5-x}Pr_xSb_{3-y}M_y$ ($M = Sn, Pb$) Electrodes for Lithium- and Sodium-Ion Batteries by Structure Disordering and CNTs Additives. *Materials* **2021**, *14*, 4331. <https://doi.org/10.3390/ma14154331>

Academic Editor:
Alessandro Dell'Era

Received: 30 June 2021
Accepted: 30 July 2021
Published: 3 August 2021

Publisher's Note: MDPI stays neutral with regard to jurisdictional claims in published maps and institutional affiliations.



Copyright: © 2021 by the authors. Licensee MDPI, Basel, Switzerland. This article is an open access article distributed under the terms and conditions of the Creative Commons Attribution (CC BY) license (<https://creativecommons.org/licenses/by/4.0/>).

1. Introduction

Intermetallics with sufficiently large interatomic voids are favorable for the insertion of lithium or sodium ions. The intermetallic compound $LaSn_3$ (AuCu₃-type) as a possible negative electrode for the lithium-ion batteries was described by Vaughey et al. [1]. The insertion of lithium atoms into octahedral voids of hexagonal Zr_5Sn_3 and RE_5M_3 ($RE = Y, La$ and Gd ; $M = Ge$ and Sn) binary phases were described earlier by us [2–4]. The crystal structure of RE_5M_3 intermetallic compounds belongs to Mn_5Si_3 -type. The RE atoms are located at $4d$ and $6g$ sites, respectively. The M components (Ge or Sn or Pb atoms) are located at the additional $6g$ site. For this binary structure, the presence of an octahedral void in the $2b$ site is typical. The incorporation of the third element (alkaline or transition metals, marked as T) into the $2b$ site leads to the realization of the RE_5TM_3 ternary phase with a Hf_5CuSn_3 structure type [5]. We detected the new ternary phase of Tb_5LiSn_3 with fully filled $2b$ site (Hf_5CuSn_3 structure type) during the systematic study of the alloys of $Tb-Li-Sn$ system [6]. The $La_5Li_xGe_3$ phase, which formed by partial incorporation (up to $x = 0.4$) of lithium atoms into octahedral voids of the La_5Ge_3 binary, was observed in $La-Li-Ge$ system [3].

The rationale for the use of high entropy alloys as electrode materials is based on the assumption defined by Jien-Wei Yeh and colleagues [7] that the presence of several (five or

more) elements in the alloy would increase the configurational entropy of mixing by an amount sufficient to overcome the enthalpies of compound formation, thereby, inhibiting the formation of potentially undesirable additional intermetallics. So, at the increasing of the number of elements in an alloy, the entropic contribution to the total free energy would overcome the enthalpic contribution and, thereby, stabilize solid solution phases [8]. Alloys of systems based on rare earth metals are prone to the formation of solid solutions, which can be both limited and unlimited. In some metallic systems, depending on the composition of the alloys, ordered intermetallic compounds, limited solid solutions, and unlimited solid solutions can be formed simultaneously [9–11]. A positive effect of component substitution on electrochemical properties was also observed for Li (Al_{1-z}Zn_z) solid solution [12].

The concept of stabilizing a crystal structure with high entropy allows us to build electrodes that can be cycled for a long time without significantly reducing the capacity. Previously, this was shown for high-entropy oxides [13] such as cathode materials and MD-HEIP intermetallics as anode materials for Li- and Na-ion batteries [14].

It is shown that increasing entropy by introducing one or more elements leads to a completely different electrochemical behavior and stability of cycles. In addition, there is a unique opportunity to fine-tune the electrochemical characteristics of high-entropy materials, using the different effects of each element on the electrochemical processes. Based on these studies, a possible reaction mechanism is proposed, which takes into account the stabilization of entropy and the maintenance of the invariance of the structure of the initial matrix throughout the cycling process.

In addition to the structural modification of the main phase of the electrode due to the substitution of components [1–14], it is also significant addition of catalysts and CNT conductive additives that improve the cyclic stability of the electrodes. According to known literature data [15–19], the carbon nanotubes (CNTs) are a good candidate material for use in Li-ion batteries due to their perfect electrochemical properties. The insertion of CNTs as a conductive additive at a lower weight loading than conventional carbon black and other graphite representatives to the electrode matrix gives the opportunity to create more quality electrodes.

Chawla et al. [20] described the inclusion of Pd catalyst in CNT cathode materials in Li-O₂ batteries and received electrochemical data with significant improvement in discharge capacities. The batteries with CNTs and Pd catalyst cycled have 35% more cycles. The activity of the germanium catalyst was investigated to improve the electrochemical performance of SnO₂/graphene nanocomposite anode material for LIBs [21].

In this study, we implemented two goals: first, we determined the effect of disordering the structure of Y_{5-x}Pr_xSb_{3-y}M_y (M = Sn, Pb) electrodes due to component substitution, and second, we determined the effect of a modifying additive (CNT) on the electrochemical activity of electrodes for LIBs and SIBs. A CNT-modified electrode shows better kinetics of Li⁺ /Na⁺ intercalation into electrodes and higher corrosion resistance in electrolyte solutions and, as a result, increases the battery life. The positive effect of these two actions leads to improved cyclic stability and increased electrode capacity up to 30% for LIBs and up to 25% for SIBs.

2. Material and Methods

2.1. Synthesis and Phase Analysis

The maximally disordered Y_{5-x}Pr_xSb_{3-y}M_y (M = Sn, Pb; 0 ≤ x, y ≤ 0.5) alloys were prepared from high purity metals: yttrium (ingot, 99.9 at.%, Sigma-Aldrich, Saint Louis, MO, USA), praseodymium (ingot, 99.9 at.%, Sigma-Aldrich, Saint Louis, MO, USA), antimony (rod, 99.99 at.%, Sigma-Aldrich, Saint Louis, MO, USA), tin (99.8%, shot, 3 mm, Sigma-Aldrich, Saint Louis, MO, USA) and lead (shot, <2 mm, 99.9%, Sigma-Aldrich, Saint Louis, MO, USA). These alloys were synthesized by arc-melting of pure metals under the argon atmosphere. The Y_{5-x}Pr_xSb_{3-y}M_y(Li/Na)_z alloys were synthesized by both thermal and electrochemical methods. For the thermal insertion of lithium and sodium into Y_{5-x}Pr_xSb_{3-y}M_y, two separate pieces of this alloy were mixed with Li or Na, respectively,

according to the aimed stoichiometry of the product and filled into tantalum crucibles under argon atmosphere that were sealed by arc-welding. For the electrochemical method, the lithiation and sodiation of $Y_{5-x}Pr_xSb_{3-y}M_y$ alloy were used. The samples synthesized by the thermal method were annealed at 670 K for 24 h. The reaction product was analyzed by X-ray powder diffraction (XRD) using Rigaku MiniFlex 600 powder diffractometer (Cu-radiation), Rigaku, Tokyo, Japan. The phase content of alloys was determined by means of a TESCAN VEGA3 electron microscope (Tescan, Brno, Czech Republic) equipped with Oxford Instruments energy dispersive X-ray analyzer, Aztec ONE system, High Wycombe, UK. In some cases, the flame photometry (Flapho-4 flame photometer, Carl Zeiss Jena, Jena, Germany) for detection of lithium was used.

2.2. Structure Refinement

Both the single crystal and powder X-ray diffraction methods were used for the investigation of the crystal structures of $Y_{5-x}Pr_xSb_{3-y}M_y$ and $Y_{5-x}Pr_xSb_{3-y}M_y(Li/Na)_z$ phases. Rietveld refinements against X-ray powder diffraction data were performed by using the FULLPROF program (version June 2020) [22]. The single crystals data were collected using an automatic four-circle Xcalibur Oxford Diffraction diffractometer (Agilent Technologies, Inc., Santa Clara, CA, USA) with CCD detector (graphite monochromatized Mo-radiation, ω -scan mode). The analytical absorption corrections were made by CrysAlisRed [23]. The crystal structure was solved by direct methods and refined using the SHELX-97 program package (Georg August University of Göttingen, Göttingen, Germany) [24,25].

Crystallographic data (CIF and structure factors) for the structures reported in this paper has been deposited with the Cambridge Crystallographic Data Centre, no. CCDC-2062904 (for $Y_{5-x}Pr_xSb_{3-y}M_yLi_z$) and CCDC-2062905 (for $Y_{5-x}Pr_xSb_{3-y}M_yNa_z$). These data can be obtained free of charge from the Cambridge Crystallographic Data Centre via http://www.ccdc.cam.ac.uk/data_request/cif (accessed on 13 February 2021) [26].

2.3. Electrochemical Investigations

Two series, each consisting of five electrodes of the corresponding compositions Y_5Sb_3 , $Y_{5-x}Pr_xSb_{3-y}Sn_y$, $Y_{5-x}Pr_xSb_{3-y}Pb_y$, $Y_{5-x}Pr_xSb_{3-y}Sn_y$ -CNT, and $Y_{5-x}Pr_xSb_{3-y}Pb_y$ -CNT were prepared for electrochemical studies. Electrodes from Y_5Sb_3 , $Y_{5-x}Pr_xSb_{3-y}Sn_y$, and $Y_{5-x}Pr_xSb_{3-y}Pb_y$ were cut from alloys or prepared by grinding of bulk alloys to powders and the following mixed in an agate mortar of 90 wt.% alloys (acting as active material) with 10 wt.% polyvinylidene fluoride (PVDF binder), and finally, these mixtures were pressed onto a stainless-steel grid (about 5 mg, coin cell type electrode 11 mm in diameter and 0.8 mm thick). The electrode with CNT catalyst ($Y_{5-x}Pr_xSb_{3-y}Sn_y$ -CNT and $Y_{5-x}Pr_xSb_{3-y}Pb_y$ -CNT) were prepared by mixing powdered alloys with carbon nanotubes in ratio 95:5, 90:10, and 85:15, respectively, and subsequently, sintering at 670 K for 48 h. The carbon nanotubes NC7000 were manufactured by Nanocyl SA (Sambreville, Belgium), which were produced through catalytic chemical vapor deposition (CCVD). Their average diameter and length were 9.5 nm and 1.5 μ m, respectively.

Subsequently, the sintering product was ground into a powder to a grain size of almost 1 μ m and mixed with 10 wt.% PVDF binder and pressed onto a stainless-steel grid. This grain size of the powder of the active phase of the anode material was due to proportionality with the grain sizes of the powder of the cathode materials, which were commercial.

The lithium-ion cells contain prepared alloy as a working electrode with Li reference and $LiCoO_2$ counter electrodes. The sodium-ion cells contain Na as a reference and Na_xCoO_2 as counter electrodes, respectively. The ethylencarbonate/dimethylcarbonate nonaqueous electrolyte, containing Li^+ or Na^+ ions were used. The anode and cathode were separated by Celgard 2320 separator (Celgrad, Charlotte, CA, USA) impregnated with an electrolyte.

Multi-cycle chronopotentiometry (CP), voltammetry (CVA) and electrochemical impedance spectroscopy (EIS) were performed in three-electrode Swagelok-type cells. All electro-

chemical measurements were carried out by means of the electrochemical station from CH Instruments (Austin, TX, USA) and 8 Channel Battery Analyzer (BST8-MA, MTI Corporation, Richmond, CA, USA). Galvanostatic charge/discharge cycles were received at $i_{\text{ch}} = 2 \text{ mA cm}^{-2}$, $i_{\text{disch}} = 1 \text{ mA cm}^{-2}$. The cyclic voltammograms were registered at scan rate = 0.001 V/s. The impedance spectra were taken on electrodes cycled between 1 and 4.5 V using a 0.001 Hz–100 kHz frequency range. To determine the values of the standard deviation for discharge capacity and parameters of EIS measurements, the experiments were repeated three times. The relative standard deviation of discharge capacities does not exceed 8%. The relative standard deviation for all EIS parameters does not exceed 12%.

3. Results and Discussion

Disordered and high-entropy alloys are suitable for the development of advanced materials with unique properties that cannot be achieved by conventional materials based only on ordered phases. High-entropy alloys can be used to create materials with high heat resistance and oxidation resistance, with improved mechanical, magnetic, and electrochemical properties. The MD and MD-HEIP were received from Y_5Sb_3 by concept based on two mechanisms: *substitution* and *insertion*. For the partial substitution of the Y atoms in crystallographic positions 4d and 6g, the Pr atoms were used, and Sn or Pb atoms were used for the partial substitution of Sb. As a result of this substitution, a MD phase of $\text{Y}_{5-x}\text{Pr}_x\text{Sb}_{3-y}\text{M}_y$ is formed. The structure of the Y_5Sb_3 binary phase contains typical empty octahedral voids in which lithium or sodium can be inserted. Moreover, atoms can be inserted in an octahedral void either thermally or electrochemically.

The results of X-ray powder diffraction and microprobe analysis show that the prepared alloys contain the hexagonal phase with Mn_5Si_3 structure type [27]. In this structure type, the binary phase Y_5Sb_3 crystallizes [28]. The X-ray powder pattern after Rietveld refinements and SEM micrographs of Y_5Sb_3 , $\text{Y}_{5-x}\text{Pr}_x\text{Sb}_{3-y}\text{Sn}_y$, and $\text{Y}_{5-x}\text{Pr}_x\text{Sb}_{3-y}\text{Pb}_y$ are presented in Figures 1 and 2a–c, respectively. The Rietveld refinements were carried out in $P6_3/mcm$ space group with the structure model corresponding to the Mn_5Si_3 structure type. The structural data for the ordered Y_5Sb_3 and disordered $\text{Y}_{5-x}\text{Pr}_x\text{Sb}_{3-y}\text{M}_y$ (M = Sn, Pb) and experimental details of the structure determination are presented in Table 1. The refined unit cell dimensions of disordered $\text{Y}_{5-x}\text{Pr}_x\text{Sb}_{3-y}\text{M}_y$ phases are increased in comparison to the binary Y_5Sb_3 ordered phase; it correlates well with atomic radii of substituting atoms.

For detailed structural analysis and to confirm that the obtained phases were MD-HEIP, a thorough high-precision structural study was performed using single-crystal X-ray methods. Two single crystals were selected from thermally synthesized and homogenized alloys $\text{Y}_{4.5}\text{Pr}_{0.5}\text{Sb}_{2.5}\text{Sn}_{0.5}\text{Li}$ and $\text{Y}_{4.5}\text{Pr}_{0.5}\text{Sb}_{2.5}\text{Sn}_{0.5}\text{Na}$ and used to completely determine the crystal structure. Initial X-ray studies showed that all single crystals had the same hexagonal structure as Hf_5CuSn_3 -type, which is a filled variant of the Mn_5Si_3 -type, in which the binary phase of Y_5Sb_3 crystallizes. Since these phases are multicomponent, it was important to more accurately determine the distribution of atoms in the crystallographic positions, which allows us to make an X-ray single crystal method. General information on the obtained structural results is summarized in Table 2. Fractional atomic coordinates and displacement parameters for $\text{Y}_{5-x}\text{Pr}_x\text{Sb}_{3-y}\text{Sn}_y\text{Li}$ and $\text{Y}_{5-x}\text{Pr}_x\text{Sb}_{3-y}\text{Sn}_y\text{Na}$ are presented in Table 3. Detailed structural refinements show that lithium and sodium can be inserted into octahedral voids.

Table 1. Crystallographic data for the Y_5Sb_3 and $Y_{5-x}Pr_xSb_{3-y}M_y$ ($M = Sn, Pb$) and experimental details of the structure determination.

1.	Phase	2.	Y_5Sb_3	3.	$Y_{5-x}Pr_xSb_{3-y}Sn_y$	4.	$Y_{5-x}Pr_xSb_{3-y}Pb_y$		
5.	Composition (at.%) from XRD	6.	$Y_{62.5}Sb_{37.5}$	7.	$Y_{57.1}Pr_{5.4}Sb_{32.2}Sn_{5.3}$	8.	$Y_{57.0}Pr_{5.5}Sb_{32.4}Pb_{5.1}$		
9.	Composition (at.%) from EPMA	10.	$Y_{62.3}Sb_{37.7}$	11.	$Y_{56.8}Pr_{5.7}Sb_{31.9}Sn_{5.6}$	12.	$Y_{57.2}Pr_{5.3}Sb_{32.5}Pb_{5.0}$		
13.	Diffractometer; radiation	14.	HZG-4a, Cu $K\alpha$	15.	HZG-4a, Cu $K\alpha$	16.	HZG-4a, Cu $K\alpha$		
17.	2θ range, deg	18.	$20 \div 100$	19.	$20 \div 100$	20.	$20 \div 100$		
21.	Step size, deg.; counting time, s.	22.	0.03, 20	23.	0.03, 20	24.	0.03, 20		
25.	Structure type	26.	alic>26. $Mn_5Si_{3.5}$	27.	alic>27. Mn_5Si_3	28.	alic>28. Mn_5Si_3		
29.	Space group	30.	$P6_3/mcm$	31.	$P6_3/mcm$	32.	$P6_3/mcm$		
33.	Pearson symbol	34.	hP16	35.	hP16	36.	hP16		
37.	Unit cell dimensions:	38.				39.			
40.	a , Å	41.	8.8892(2)	42.	9.0325(1)	43.	9.0418(2)		
44.	c , Å	45.	6.3256(1)	46.	6.5958(1)	47.	6.6023(1)		
48.	alic>48. V , Å ³	49.	432.87(2)	50.	466.03(1)	51.	467.45(2)		
52.	Reliability factors:	53.				54.			
55.	R_F (%); R_B (%)	56.	6.02, 7.83	57.	5.17, 6.06	58.	5.33, 7.28		
59.	R_P (%)	60.	4.92	61.	3.17	62.	3.23		
63.	R_{wp} (%)	64.	8.19	65.	4.65	66.	5.30		
67.	χ^2	68.	2.13	69.	1.07	70.	0.97		
71.	Atomic parameters (xyz):	72.	$4d$	75.	$Y1\ 1/3\ 2/3\ 0$	78.	$(Y/Pr)1\ 1/3\ 2/3\ 0$	81.	$(Y/Pr)1\ 1/3\ 2/3\ 0$
		73.	$6g$	76.	$Y2\ 0.2363(1)\ 0\ 1/4$	79.	$(Y/Pr)2\ 0.2406(1)\ 0\ 1/4$	82.	$(Y/Pr)2\ 0.2438(1)\ 0\ 1/4$
		74.	$6g$	77.	$Sb\ 0.5997(2)\ 0\ 1/4$	80.	$(Sb/Sn)\ 0.6036(2)\ 0\ 1/4$	83.	$(Sb/Pb)\ 0.6062(2)\ 0\ 1/4$

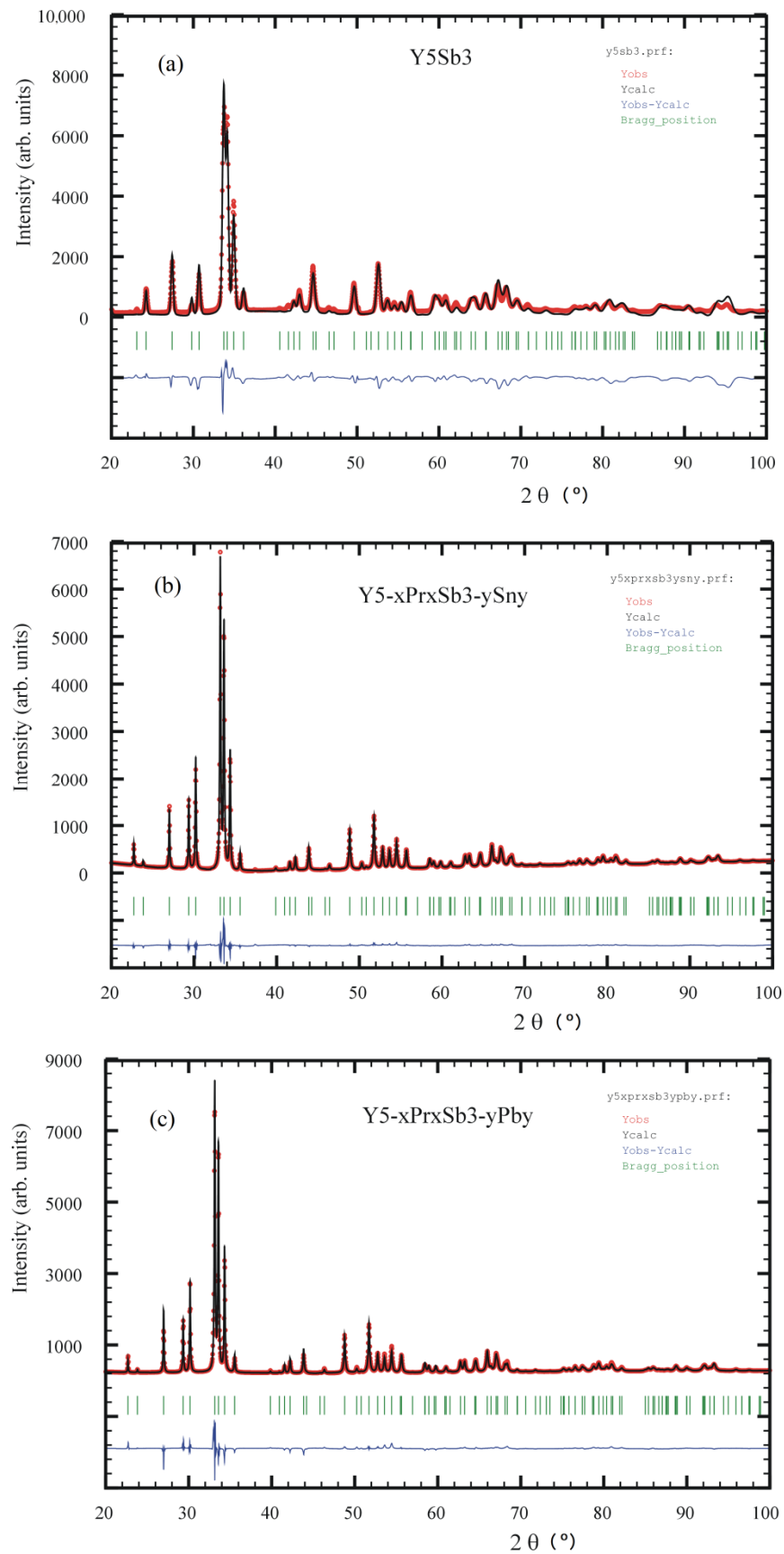


Figure 1. Observed (circles), calculated (line), and difference (bottom line) x-ray powder diffraction patterns for of Y_5Sb_3 (a), $Y_{5-x}Pr_xSb_3-ySn_y$ (b), and $Y_{5-x}Pr_xSb_3-yPb_y$ (c) alloys.

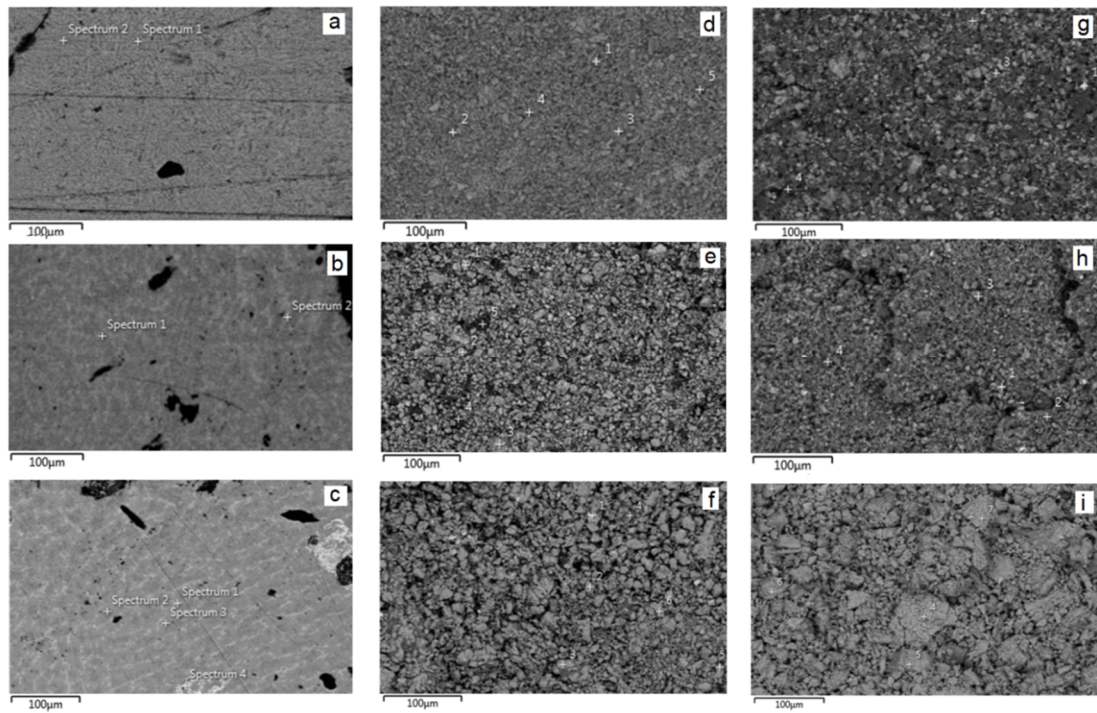


Figure 2. SEM images of Y_5Sb_3 (a), $Y_{5-x}Pr_xSb_{3-y}Sn_y$ (b), and $Y_{5-x}Pr_xSb_{3-y}Bi_y$ (c) alloys and images of these alloys after lithiation (d–f) and sodiation (g–i), respectively.

Table 2. Crystallographic data for $Y_{5-x}Pr_xSb_{3-y}Sn_yLi$ and $Y_{5-x}Pr_xSb_{3-y}Sn_yNa$ single crystals and experimental details of the structure determination.

84. Phase	85. $Y_{5-x}Pr_xSb_{3-y}Sn_yLi$	86. $Y_{5-x}Pr_xSb_{3-y}Sn_yNa$
87. Formula	88. $Y_{4.5}Pr_{0.5}Sb_{2.5}Sn_{0.5}Li$	89. $Y_{4.5}Pr_{0.5}Sb_{2.5}Sn_{0.5}Na$
90. Structure type	91. Hf_5CuSn_3	92. Hf_5CuSn_3
93. Formula weight (g/mol)	94. 841.22	95. 857.27
96. Space group	97. $P6_3/mcm$	98. $P6_3/mcm$
99. Pearson symbol	100. hP18	101. hP18
102. Crystal dimensions (mm^3)	103. $0.04 \times 0.05 \times 0.09$	104. $0.03 \times 0.04 \times 0.08$
105. Unit cell dimensions:	106.	107.
108. a , Å	109. 9.0614(1)	110. 9.0978(1)
111. c , Å	112. 6.6192(1)	113. 6.6599(1)
114. V , Å ³	115. 470.68(1)	116. 477.39(1)
117. Calculated density (D_{calc} , $g \cdot cm^{-3}$)	118. 5.935	119. 5.964
120. Absorption coefficient (μ , mm^{-1})	121. 38.203	122. 37.714
123. Scan mode	124. Ω	125. ω
126. Theta range for data collection (deg.)	127. 2.60–26.69	128. 2.59–26.31
129. $F(000)$	130. 721	131. 737
132. Range in hkl	133. $-11 \leq h \leq 11, 134. -11 \leq k \leq 11, 135. -7 \leq l \leq 7$	136. $-11 \leq h \leq 11, 137. -11 \leq k \leq 11, 138. -7 \leq l \leq 7$
139. Total no. reflections	140. 1544	141. 1522
142. Reflections with $I > 2\sigma(I)$	143. 190 ($R_{sigma} = 0.0114$)	144. 189 ($R_{sigma} = 0.0180$)
145. Data/parameters	146. 190/12	147. 189/13
148. Goodness-of-fit on F^2	149. 1.144	150. 1.169
151. Final R indices [$I > 2\sigma(I)$]	152. $R_1 = 0.0341$	153. $R_1 = 0.0476$
154.	$wR_2 = 0.0936$	155. $wR_2 = 0.1296$
156. Largest diff. peak/hole ($e/\text{Å}^3$)	157. 2.204/−1.901	158. 2.622/−1.981

Table 3. Fractional atomic coordinates and displacement parameters for $Y_{5-x}Pr_xSb_{3-y}Sn_yLi$ and $Y_{5-x}Pr_xSb_{3-y}Sn_yNa$ (\AA^2).

159. Atom	160. Site	161. x/a	162. y/b	163. z/c	164. U_{iso}^*/U_{eq}	165. Occ. (<1)
166. $Y_{5-x}Pr_xSb_{3-y}Sn_yLi$						
167. Y1	168. 6g	169. 0.2696(2)	170. 0.2696(2)	171. 1/4	172. 0.0233(6)	173. 0.80
174. Pr1	175. 6g	176. 0.2696(2)	177. 0.2696(2)	178. 1/4	179. 0.0233(6)	180. 0.20
181. Y2	182. 4d	183. 2/3	184. 1/3	185. 0	186. 0.0180(6)	187. 0.88
188. Pr2	189. 4d	190. 2/3	191. 1/3	192. 0	193. 0.0180(6)	194. 0.12
195. Sb1	196. 6g	197. 0.63128(12)	198. 0.63128(12)	199. 1/4	200. 0.0084(5)	201. 0.80
202. Sn1	203. 6g	204. 0.63128(12)	205. 0.63128(12)	206. 1/4	207. 0.0084(5)	208. 0.20
209. Li1	210. 2b	211. 0	212. 0	213. 0	214. 0.002 *	215. 1.00
216.	U^{11}	217. U^{22}	218. U^{33}	219. U^{12}	220. U^{13}	221. U^{23}
222. Y1	223. 0.0224(7)	224. 0.0224(7)	225. 0.0256(11)	226. 0.0116(8)	227. 0	228. 0
229. Pr1	230. 0.0224(7)	231. 0.0224(7)	232. 0.0256(11)	233. 0.0116(8)	234. 0	235. 0
236. Y2	237. 0.0171(7)	238. 0.0171(7)	239. 0.0196(13)	240. 0.0086(3)	241. 0	242. 0
243. Pr2	244. 0.0171(7)	245. 0.0171(7)	246. 0.0196(13)	247. 0.0086(3)	248. 0	249. 0
250. Sb1	251. 0.0078(5)	252. 0.0078(5)	253. 0.0110(7)	254. 0.0049(5)	255. 0	256. 0
257. Sn1	258. 0.0078(5)	259. 0.0078(5)	260. 0.0110(7)	261. 0.0049(5)	262. 0	263. 0
264. $Y_{5-x}Pr_xSb_{3-y}Sn_yNa$						
265. Y1	266. 6g	267. 0.2704(3)	268. 0.2704(3)	269. 1/4	270. 0.0261(9)	271. 0.80
272. Pr1	273. 6g	274. 0.2704(3)	275. 0.2704(3)	276. 1/4	277. 0.0261(9)	278. 0.20
279. Y2	280. 4d	281. 2/3	282. 1/3	283. 0	284. 0.0261(10)	285. 0.76
286. Pr2	287. 4d	288. 2/3	289. 1/3	290. 0	291. 0.0261(10)	292. 0.24
293. Sb1	294. 6g	295. 0.63151(18)	296. 0.63151(18)	297. 1/4	298. 0.0113(8)	299. 0.80
300. Sn1	301. 6g	302. 0.63151(18)	303. 0.63151(18)	304. 1/4	305. 0.0113(8)	306. 0.20
307. Na1	308. 2b	309. 0	310. 0	311. 0	312. 0.008 *	313. 0.98
314.	U^{11}	315. U^{22}	316. U^{33}	317. U^{12}	318. U^{13}	319. U^{23}
320. Y1	321. 0.0267(12)	322. 0.0267(12)	323. 0.0280(16)	324. 0.0152(12)	325. 0	326. 0
327. Pr1	328. 0.0267(12)	329. 0.0267(12)	330. 0.0280(16)	331. 0.0152(12)	332. 0	333. 0
334. Y2	335. 0.0241(11)	336. 0.0241(11)	337. 0.031(2)	338. 0.0121(6)	339. 0	340. 0
341. Pr2	342. 0.0241(11)	343. 0.0241(11)	344. 0.031(2)	345. 0.0121(6)	346. 0	347. 0
348. Sb1	349. 0.0102(9)	350. 0.0102(9)	351. 0.0140(11)	352. 0.0053(7)	353. 0	354. 0
355. PB1	356. 0.0102(9)	357. 0.0102(9)	358. 0.0140(11)	359. 0.0053(7)	360. 0	361. 0

U_{eq} is defined as one third of the trace of the orthogonalized U_{ij} tensor. The anisotropic displacement factor exponent takes the form: $U_{ij} = -2\pi^2[(h^2a^*)^2U_{11} + \dots + 2hka^*b^*U_{12}]$. $U_{13} = U_{23} = 0$.

The structural feature of these phases based on the possibility of insertion/deinsertion of lithium and sodium atoms into octahedral voids prompted the study of the possibility of carrying out these processes using electrochemical methods. The insertion of lithium or sodium atoms significantly increases the volume of the unit cell, more significantly along the lattice period c , since in this direction, the octahedron expands more during the insertion of atoms (Figure 3). At the insertion of Li into octahedra, the volume of the unit cell increases by 4.65 \AA^3 , and there are even greater changes up to 11.36 \AA^3 when sodium atoms are inserted.

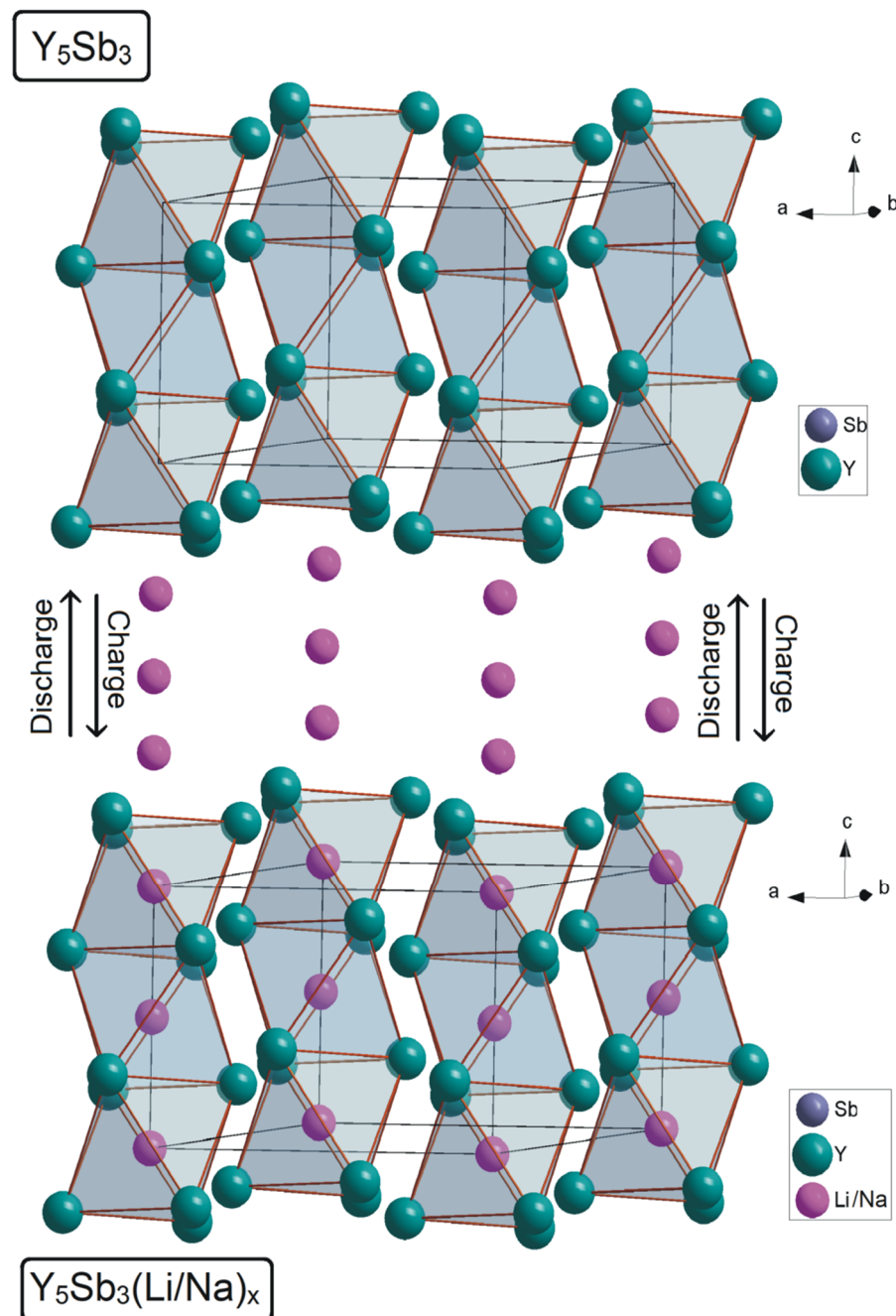


Figure 3. Scheme of insertion of the lithium or sodium atoms into octahedral voids.

After several initial cycles of electrochemical lithiation/delithiation, as well as sodiation/desodiation of disk electrodes that were cut from the alloy, their amorphization was observed (Figure 2d–i), and their capacity decreased slightly. After 5–8 cycles of activation, the electrodes stabilized and could continue to operate for many cycles without significant loss of capacity. There are no significant differences when using electrodes that were made by pressing powders from crushed alloys. It should be noted that the electrodes from the ordered binary phase Y_5Sb_3 have a discharge capacity in the range of $200 \text{ mAh} \cdot \text{g}^{-1}$ (for LIBs) and $120 \text{ mAh} \cdot \text{g}^{-1}$ (for SIBs), respectively (Figure 4). The use of electrodes from the MD phases increases the discharge capacitance for both LIBs and SIBs by almost 10%. Moreover, slightly higher values of capacitance have electrodes in which the Sb atoms are replaced by Sn, in comparison with electrodes in which the Sb are replaced by Pb atoms.

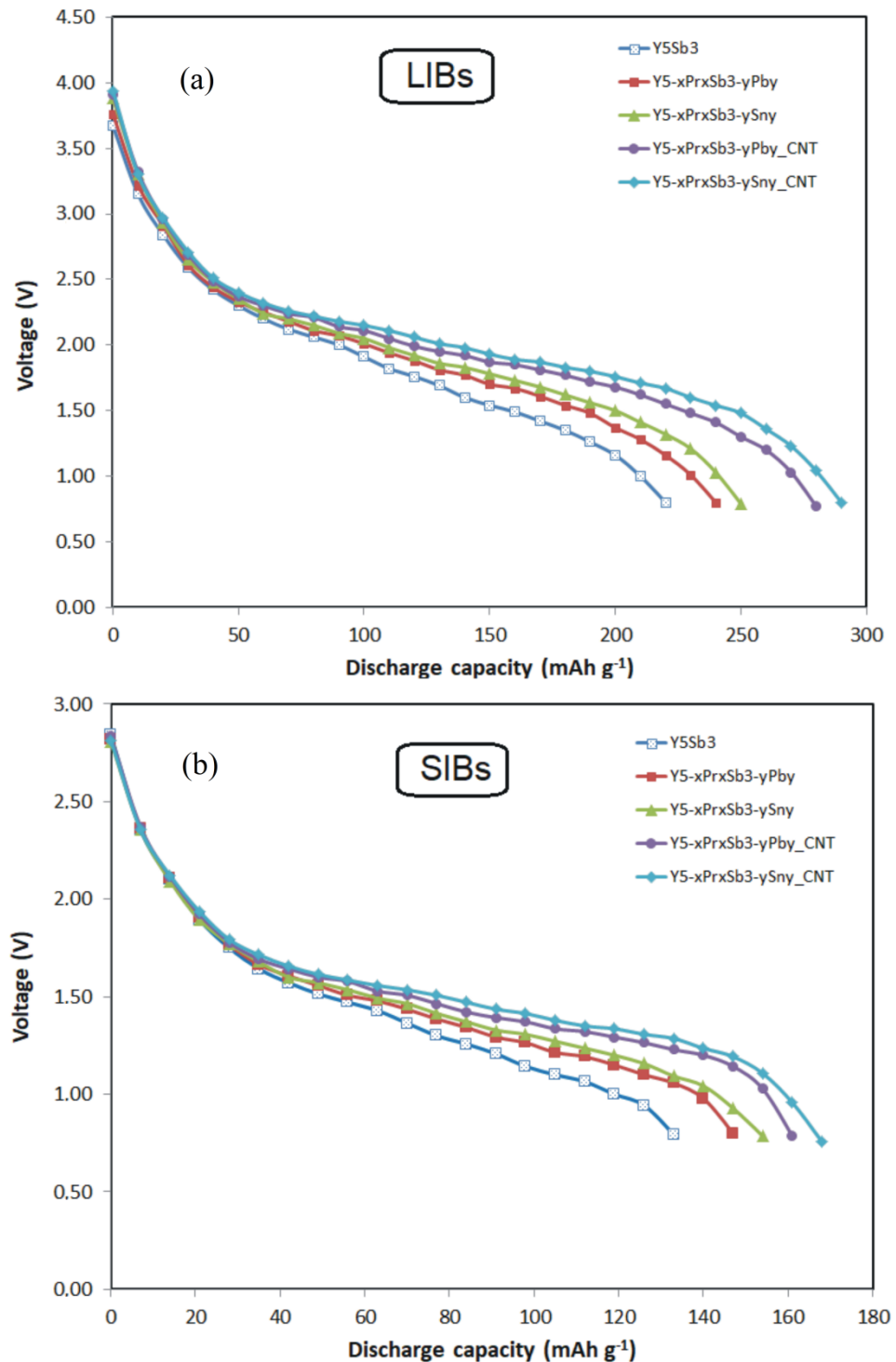


Figure 4. The galvanostatic discharge curve for LIBs (a) and SIBs (b).

The next important step was the modification of the electrodes by carbon nanotubes in order to increase their capacity and improve cyclic stability. This modification was performed for MD phases of $Y_{5-x}Pr_xSb_{3-y}Sn_y$ and $Y_{5-x}Pr_xSb_{3-y}Pb_y$. Different amounts of CNT were added, namely 5, 10, and 15 wt.% to alloys with subsequent mixing, pressing, and sintering. For example, Figure 5 shows the SEM images of the initial alloy, nanotubes, and the product of their sintering. It is seen that the nanotubes wrap the grains of the alloy, filling the intergranular space.

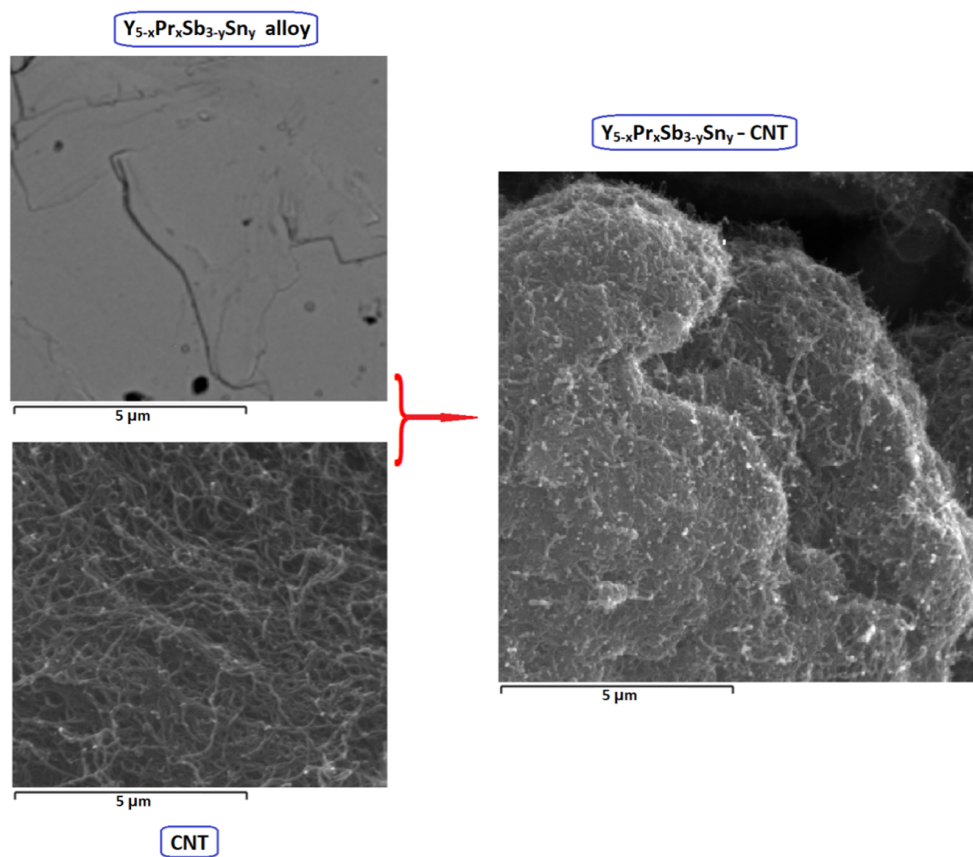


Figure 5. SEM images of initial $Y_{5-x}Pr_xSb_{3-y}Sn_y$ alloy, CNT, and modified $Y_{5-x}Pr_xSb_{3-y}Sn_y$ -CNT after sintering.

Electrochemical studies have shown that the optimal amount of CNT is 10 wt.%. It has been experimentally established that if the content of carbon nanotubes in the electrodes exceeds 10 wt.%, for example, 15 wt.%, the capacity and cyclic characteristics of the electrodes begin to deteriorate due to the formation of grains of carbide phases during sintering. It is also important to ensure the mechanical stability of the electrodes so that they do not crack during numerous charge–discharge cycles. This is realized by adding a binder material, the optimal amount of which was 10 wt.%. The addition of CNTs and PVDF binder to electrodes improved capacity and their cycles' stability. The CNTs provided diffusion pathways for Li^+ or Na^+ ions to most of the grains inside the material, improving charge/discharge kinetics, and the PVDF binder provided good adhesion between the electrode materials and current collectors, giving excellent electrochemical, mechanical, and thermal stability of electrodes. Modification of alloys with carbon nanotubes allowed us to significantly increase the discharge capacity of both types of batteries as LIBs and SIBs (Figure 4). Modification of $Y_{5-x}Pr_xSb_{3-y}M_y$ ($M = Sn, Pb$) alloys by carbon nanotubes allowed us to significantly increase the discharge capacity of both types of batteries, which reached $280 \text{ mAh} \cdot \text{g}^{-1}$ (for LIBs) and $160 \text{ mAh} \cdot \text{g}^{-1}$ (for SIBs), respectively. These maximum capacities are for $Y_{5-x}Pr_xSb_{3-y}Sn_y$ alloy electrodes in which antimony is partially replaced by tin. For $Y_{5-x}Pr_xSb_{3-y}Pb_y$ alloys in which antimony is replaced by lead, these capacities are slightly smaller and are $270 \text{ mAh} \cdot \text{g}^{-1}$ (for LIBs) and $155 \text{ mAh} \cdot \text{g}^{-1}$ (for SIBs), respectively. The study of cyclic stability shows that for CNT-modified electrodes after 50 cycles of charge–discharge, capacity decreases by no more than 8% (Figure 6).

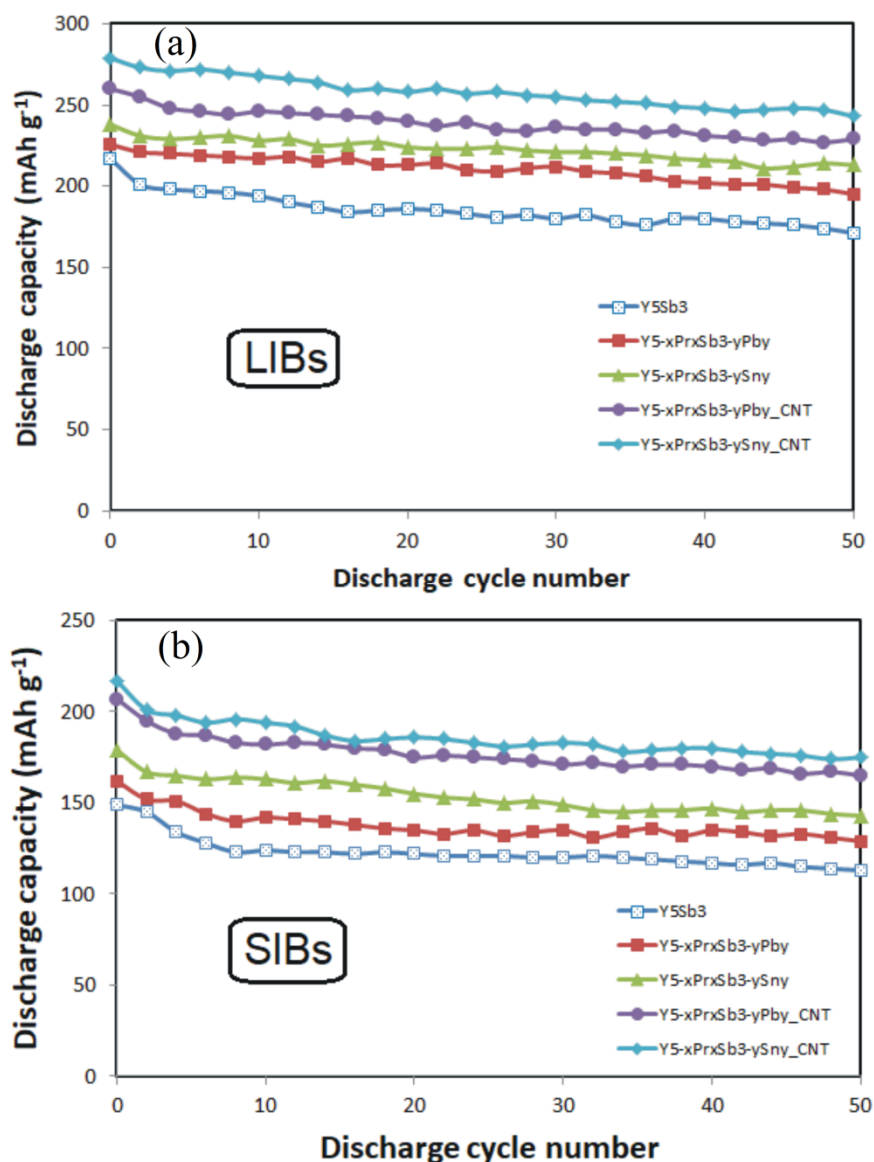


Figure 6. Specific capacities vs. cycle number of the tested alloys for LIBs (a) and SIBs (b).

The analysis potentiodynamic polarization curves (Figure 7) show that tested Y₅Sb₃, Y_{5-x}Pr_xSb_{3-y}M_y (M = Sn, Pb), and Y_{5-x}Pr_xSb_{3-y}M_y-CNT electrodes passivate in LiPF₆ based ethylencarbonate/dimethylcarbonate electrolyte, electrolyte solution, and their passivation range extends from +1.07 V to +0.70 V. The electrode corrosion potential (E_{corr}) is equal to +1.07 V for Y₅Sb₃ and shifts to +0.97 V for Y_{5-x}Pr_xSb_{3-y}Pb_y and +0.84 V for Y_{5-x}Pr_xSb_{3-y}Sn_y. For the catalyst activated by CNT, Y_{5-x}Pr_xSb_{3-y}Pb_y-CNT and Y_{5-x}Pr_xSb_{3-y}Sn_y-CNT electrodes, the E_{corr} shifts to +0.77 V and +0.70 V, respectively, and these shifts indicate an increase of corrosion resistance in the electrolyte solution, which causes a higher specific capacity and better cyclic stability.

Figure 8 shows the Nyquist plot from electrochemical impedance spectroscopy (EIS) data of Y₅Sb₃, Y_{5-x}Pr_xSb_{3-y}M_y (M = Sn, Pb), and Y_{5-x}Pr_xSb_{3-y}M_y-CNT (M = Sn, Pb) electrodes for both LIBs and SIBs. The semi-circle areas correspond to the charge transfer limitation. Generally, the kinetics of Li⁺ ions intercalation into electrodes is faster than Na⁺ because of the smaller radius and lighter mass of Li⁺ compared to Na⁺, resulting in smaller charge transfer resistances in the LIBs (Figure 8a) than in the SIBs (Figure 8b). As shown in Figure 8 for LIBs, the semi-circle areas of Y_{5-x}Pr_xSb_{3-y}M_y-CNT (M = Sn, Pb) electrodes are smaller than those of the Y₅Sb₃ and Y_{5-x}Pr_xSb_{3-y}M_y, which demonstrates

that the charge-transfer reaction is facilitated for the modified electrode. Similar behavior of these electrodes is observed for SIBs, but the higher values of the resistances indicate that the processes of charge transfer in this system are more difficult.

The electrochemical lithiation and sodiation of $Y_{5-x}Pr_xSb_{3-y}M_y$ phase can be written, respectively, as:

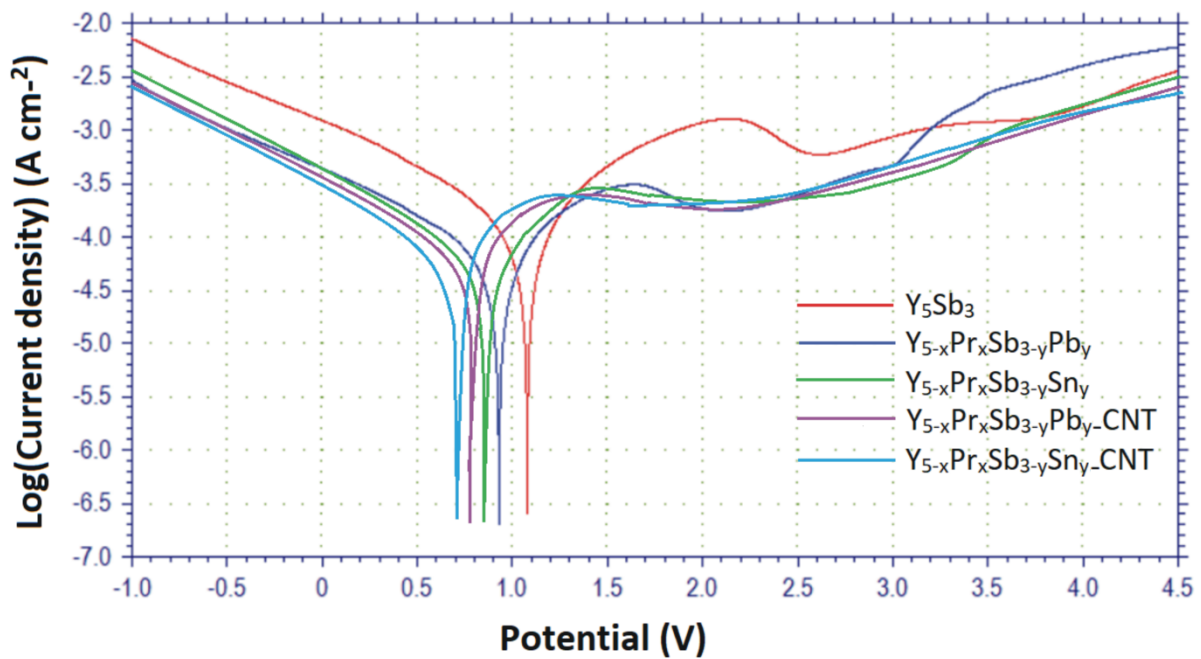
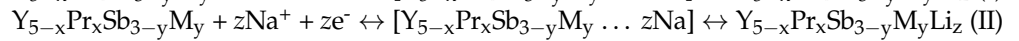
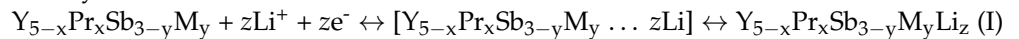


Figure 7. Potentiokinetic polarization curves of the tested alloys for LIBs.

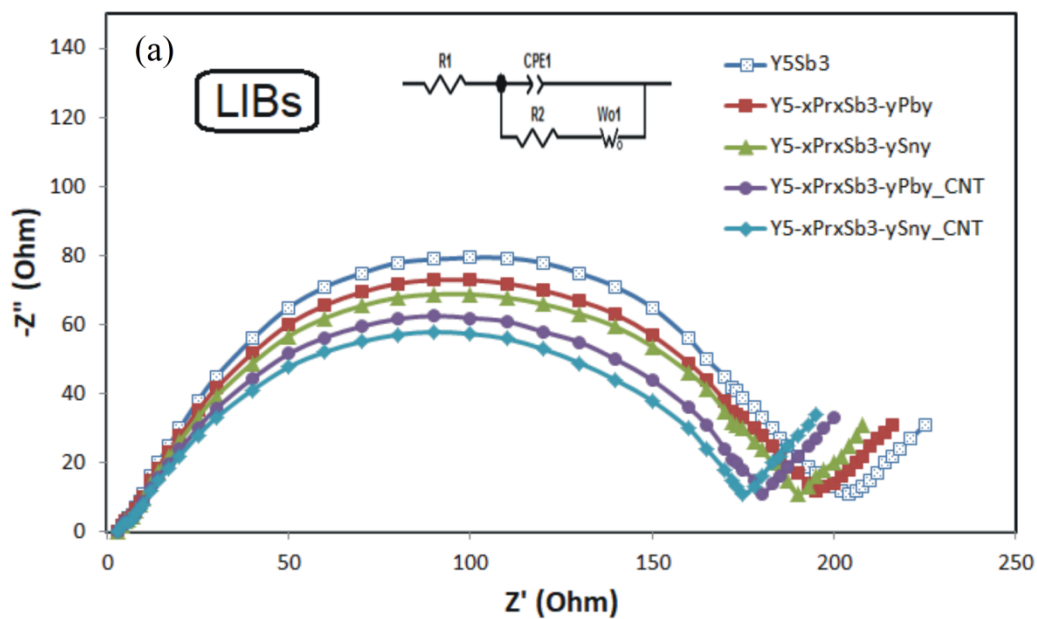


Figure 8. Cont.

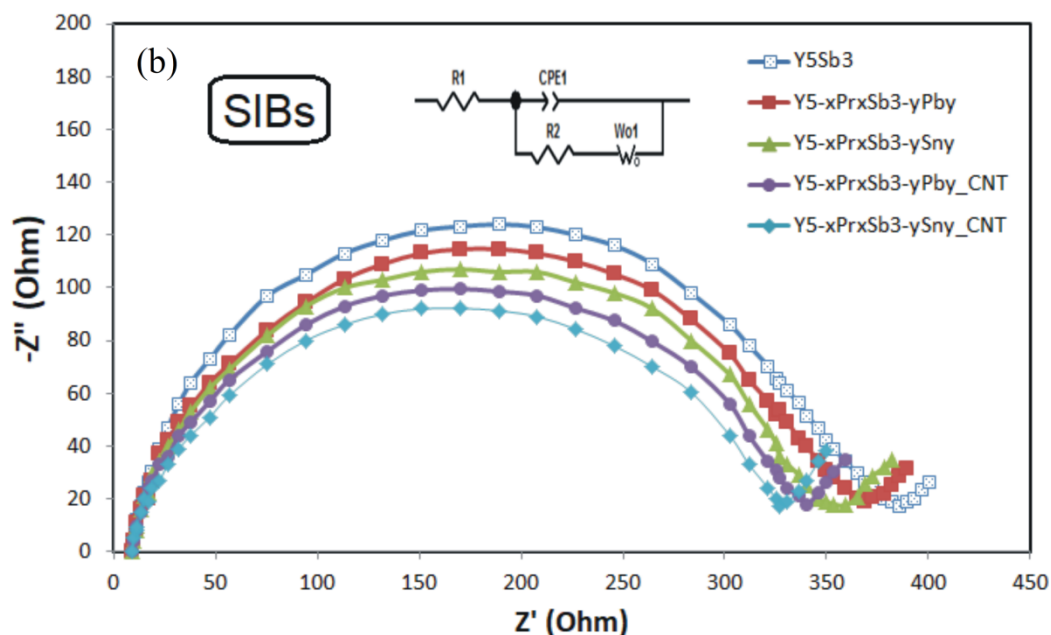


Figure 8. Nyquist plot from electrochemical impedance spectroscopy (EIS) data of the tested alloys for LIBs (a) and SIBs (b). EIS data analyzed by fitting to an equivalent electrical circuit scheme (inset) in which R1 is the electrolyte solution resistance, R2 is the charge transfer resistance, CPE1 is the double-layer capacitance, and Wo1 is related to the diffusion-controlled Warburg impedance.

CNT additives fill the intergranular space during sintering and improve the electrical connectivity within the electrode, thus, improving capacity by connecting and maintaining more electron conduction pathways between the active material and the current collector and then, finally, increasing the specific capacities and cycle stability of electrodes.

4. Conclusions

The maximally disordered $Y_{5-x}Pr_xSb_{3-y}M_y$ ($M = Sn, Pb$) phases with stable hexagonal Mn_5Si_3 structure type were prepared and investigated as the anode materials for LIBs and SIBs. During the electrochemical lithiation and sodiation, the formation of $Y_{5-x}Pr_xSb_{3-y}M_yLi_z$ and $Y_{5-x}Pr_xSb_{3-y}M_yNa_z$ maximally disordered–high entropy intermetallic phases, as the result of the insertion of Li/Na into octahedral voids, were observed. Carbon nanotubes are an effective additive to improve the cycle stability of the $Y_{5-x}Pr_xSb_{3-y}M_y$ ($M = Sn, Pb$) anodes for lithium-ion and sodium-ion batteries. Modification of $Y_{5-x}Pr_xSb_{3-y}M_y$ ($M = Sn, Pb$) alloys by structure disordering and carbon nanotube additives allowed us to significantly increase the discharge capacity of both types of batteries, which reached $280 \text{ mAh} \cdot \text{g}^{-1}$ (for LIBs) and $160 \text{ mAh} \cdot \text{g}^{-1}$ (for SIBs), respectively. A CNT-modified electrode also shows higher corrosion resistance in electrolyte solutions and, as a result, demonstrates an increased battery life. The effect of the addition of CNTs and PVDF binder on the improvement of capacity and cycle stability of electrodes is due to the following factors: CNTs provide diffusion pathways for Li^+ or Na^+ ions to most of the grains inside the material, improving charge/discharge kinetics; PVDF provides good adhesion between the electrode materials and current collectors, giving excellent electrochemical, mechanical, and thermal stability of electrodes.

Author Contributions: Conceptualization, V.P. and W.C.; methodology, V.P.; software, N.P. and DK; validation, V.P. and W.C.; investigation, V.P., N.P., D.K., A.B. and K.K.; writing—original draft preparation, V.P. and W.C.; visualization, N.P., A.B. and K.K.; supervision, V.P. All authors have read and agreed to the published version of the manuscript.

Funding: Funding for this research was provided by: National Science Centre, Poland (No. 2017/25/B/ST8/02179) and partially by grant 2015/19/N/ST8/03922. Partial studies also were conducted under grant German Academic Exchange Service (DAAD).

Institutional Review Board Statement: Not applicable.

Informed Consent Statement: Not applicable.

Data Availability Statement: Data is contained within the article.

Conflicts of Interest: The authors declare no conflict of interest.

References

1. Vaughey, J.T.; Thackeray, M.M.; Shin, D.; Wolverton, C. Studies of LaSn_3 as a Negative Electrode for Lithium-Ion Batteries. *J. Electrochem. Soc.* **2009**, *156*, 536–540. [CrossRef]
2. Balinska, A.; Kordan, V.; Misztal, R.; Pavlyuk, V. Electrochemical and thermal insertion of lithium and magnesium into Zr_5Sn_3 . *J. Solid State Electrochem.* **2015**, *19*, 2481–2490. [CrossRef]
3. Pavlyuk, V.; Stetskiv, A.; Rozdzyńska-Kielbik, B. The isothermal section of the phase diagram of Li–La–Ge ternary system at 400° C. *Intermetallics* **2013**, *43*, 29–37. [CrossRef]
4. Stetskiv, A.; Kordan, V.; Tarasiuk, I.; Zelinska, O.; Pavlyuk, V. Structural peculiarities and electrochemical properties of R_5M_3 (R = La, Gd; M = Ge, Sn) doped by lithium. *Chem. Met. Alloys* **2014**, *7*, 106–111. [CrossRef]
5. Rieger, W.; Nowotny, H.; Benesovsky, F. Phasen mit oktaedrischen Bauelementen des Übergangsmetalls. *Monatsh Chem.* **1965**, *96*, 232–241. [CrossRef]
6. Stetskiv, A.; Tarasiuk, I.; Misztal, R.; Pavlyuk, V. Pentaterybium lithium tristannide, Tb_5LiSn_3 . *Acta Cryst. E* **2011**, *67*, i61. [CrossRef] [PubMed]
7. Yeh, J.W.; Chen, S.K.; Lin, S.J.; Gan, J.Y.; Chin, T.S.; Shun, T.T.; Tsau, C.H.; Chang, S.Y. Nanostructured high-entropy alloys with multiple principal elements: Novel alloy design concepts and outcomes. *Adv. Eng. Mater.* **2004**, *6*, 299–303. [CrossRef]
8. George, E.P.; Raabe, D.; Ritchie, R.O. High-entropy alloys. *Nat. Rev. Mater.* **2019**, *4*, 515–534. [CrossRef]
9. Pavlyuk, V.V.; Opainych, I.M.; Bodak, O.I.; Pałasińska, T.; Rożdżyńska, B.; Bala, H. Interaction of the component in the La–Ni–Zn System. *Pol. J. Chem.* **1997**, *71*, 309–313.
10. Pavlyuk, V.; Marciniak, B.; Rozycka-Sokolowska, E. The isothermal section of the phase diagram of Ce–Mg–Zn ternary system at 470 K. *Intermetallics* **2012**, *20*, 8–15. [CrossRef]
11. Pavlyuk, V.; Solokha, P.; Zelinska, O.; Paul-Boncour, V.; Nowik-Zajac, A. $\text{Ce}_{20}\text{Mg}_{19}\text{Zn}_{81}$ —a new structure type with a giant cubic cell. *Acta Cryst. C* **2008**, *64*, i50–i52. [CrossRef]
12. Chumak, I.; Dmytriv, G.; Pavlyuk, V.; Oswald, S.; Eckert, J.; Trill, H.; Eckert, H.; Pauly, H.; Ehrenberg, H. $\text{Li}(\text{Al}_{1-z}\text{Zn}_z)$ alloys as anode materials for rechargeable Li-ion batteries. *J. Mater. Res.* **2010**, *25*, 1492–1499. [CrossRef]
13. Sarkar, A.; Velasco, L.; Wang, D.; Wang, Q.; Talasila, G.; de Biasi, L.; Kübel, K.; Brezesinski, T.; Bhattacharya, S.S.; Hahn, Y.; et al. High entropy oxides for reversible energy storage. *Nat. Commun.* **2018**, *9*, 3400. [CrossRef]
14. Pavlyuk, V.; Balinska, A.; Rozdzyńska-Kielbik, B.; Pavlyuk, N.; Dmytriv, G.; Stetskiv, A.; Indris, S.; Schwarz, B.; Ehrenberg, H. New maximally disordered-high entropy intermetallic phases (MD-HEIP) of the $\text{Gd}_{1-x}\text{La}_x\text{Sn}_{2-y}\text{Sb}_y\text{M}_z$ (M = Li, Na, Mg): Synthesis, structure and some properties. *J. Alloys Compd.* **2020**, *838*, 155643. [CrossRef]
15. Landi, B.J.; Ganter, M.J.; Cress, C.D.; DiLeo, R.A.; Raffaele, R.P. Carbon nanotubes for lithium ion batteries. *Energy Environ. Sci.* **2009**, *2*, 638–654. [CrossRef]
16. Frackowiak, E.; Beguin, F. Electrochemical Storage of Energy in Carbon Nanotubes and Nanostructured Carbons. *Carbon* **2002**, *40*, 1775–1787. [CrossRef]
17. Chen, W.X.; Lee, J.Y.; Liu, Z. The nanocomposites of carbon nanotube with Sb and $\text{SnSb}_{0.5}$ as Li-ion battery anodes. *Carbon* **2003**, *41*, 959–966. [CrossRef]
18. Yang, S.; Song, H.; Chen, X.; Okotrub, A.V.; Bulusheva, L.G. Electrochemical performance of arc-produced carbon nanotubes as anode material for lithium-ion batteries. *Electrochem. Acta* **2007**, *52*, 5286–5293. [CrossRef]
19. Lin, K.; Xu, Y.; He, G.; Wang, X. The kinetic and thermodynamic analysis of Li ion in multi-walled carbon nanotubes. *Mater. Chem. Phys.* **2006**, *99*, 190–196. [CrossRef]
20. Chawla, N.; Chamaani, A.; Safa, M.; El-Zahab, B. Palladium-Filled Carbon Nanotubes Cathode for Improved Electrolyte Stability and Cyclability Performance of Li–O₂ Batteries. *J. Electrochem. Soc.* **2017**, *164*, A6303–A6307. [CrossRef]
21. Zhu, Y.G.; Wang, Y.; Han, Z.J.; Shi, Y.; Wong, J.I.; Huang, Z.X.; Ostrikov, K.K.; Yang, H.Y. Catalyst engineering for lithium ion batteries: The catalytic role of Ge in enhancing the electrochemical performance of $\text{SnO}_2(\text{GeO}_2)_{0.13}/\text{G}$ anodes. *Nanoscale* **2014**, *6*, 15020–15028. [CrossRef]
22. Rodriguez-Carvajal, J. Recent advances in magnetic structure determination by neutron powder diffraction. *Physica B* **1993**, *192*, 55–69. [CrossRef]
23. CrysAlis PRO. Yarnton, Oxfordshire, UK Ltd. Agilent Technologies, England. Version 1.171.32.18. Available online: https://www.agilent.com/cs/library/usermanuals/public/CrysAlis_Pro_User_Manual.pdf (accessed on 18 October 2011).
24. Sheldrick, G.M. *SHELXS, Program for the Solution of Crystal Structures*; University of Goettingen: Goettingen, Germany, 1997.

25. Sheldrick, G.M. *SHELXL-97, Program for Crystal Structure Refinement*; University of Goettingen: Goettingen, Germany, 1997.
26. Crystallographic Data (CIF and Structure Factors) for the Structures Reported in This Paper Has Been Deposited with the Cambridge Crystallographic Data Centre, No. CCDC-2062904 (for $Y_{5-x}Pr_xSb_{3-y}M_yLi_z$) and CCDC-2062905 (for $Y_{5-x}Pr_xSb_{3-y}M_yNa_z$). Available online: http://www.ccdc.cam.ac.uk/data_request/cif (accessed on 13 February 2021).
27. Aronsson, B. A note on the compositions and crystal structures of MnB_2 , Mn_3Si , Mn_5Si_3 and $FeSi_2$. *Acta Chem. Scand.* **1960**, *14*, 1414–1418. [[CrossRef](#)]
28. Kozlov, A.Y.; Pavlyuk, V.V. Investigation of the interaction of the components in the Y-Si-Sb system at 670 K. *J. Alloys Compd.* **2004**, *370*, 192–197. [[CrossRef](#)]